J. Fluid Mech. (2013), *vol.* 714, *pp.* 127–151.
doi:10.1017/jfm.2012.462

Fluxes through steady chimneys in a mushy layer during binary alloy solidification

David W. Rees Jones† and M. Grae Worster

Institute of Theoretical Geophysics, Department of Applied Mathematics and Theoretical Physics, University of Cambridge, Wilberforce Road, Cambridge CB3 0WA, UK

(Received 10 April 2012; revised 24 July 2012; accepted 17 September 2012)

Solute transport within solidifying binary alloys occurs predominantly by convection from narrow liquid chimneys within a porous mushy layer. We develop a simple model that elucidates the dominant structure and driving forces of the flow, which could be applied to modelling brine fluxes from sea ice, where a cheaply implementable approach is essential. A horizontal density gradient within the mushy layer in the vicinity of the chimneys leads to baroclinic torque which sustains the convective flow. In the bulk of the mushy layer, the isotherms are essentially horizontal. In this region, we impose a vertically linear temperature field and immediately find that the flow field is a simple corner flow. We determine the strength of this flow by finding a similarity solution to the governing mushy-layer equations in an active region near the chimney. We also determine the corresponding shape of the chimney, the vertical structure of the solid fraction and the interstitial flow field. We apply this model first to a periodic, planar array of chimneys and show analytically that the solute flux through the chimneys is proportional to a mush Rayleigh number. Secondly we extend the model to three dimensions and find that an array of chimneys can be characterized by the average drainage area alone. Therefore we solve the model in an axisymmetric geometry and find new, sometimes nonlinear, relationships between the solute flux, the Rayleigh number and the other dimensionless parameters of the system.

Key words: convection in porous media, sea ice, solidification/melting

1. Introduction

In the depths of the polar winter, vast tracts of the ocean freeze, forming or thickening a layer of porous sea ice. The brine in the pores of the ice becomes increasingly salty as the water continues to solidify. This creates a density gradient that drives convection within and out of the ice, through vertical brine channels. Of the mechanisms for salt fluxes from sea ice described by Untersteiner (1968), convection within the ice is dominant, at least during the winter growth season (Notz & Worster 2009). However, this dynamic process is inadequately represented in current models of sea ice. We aim to address this deficiency by developing a simple model that is cheap to implement.

This kind of convective behaviour is generic to the solidification of two-component solutions called binary alloys, in which the vertical channels are often called

† Email address for correspondence: dwr29@cam.ac.uk

chimneys (Copley *et al.* 1970). When a binary alloy solidifies, a mushy layer usually forms, which is a reactive porous medium where solid crystals co-exist in thermodynamic equilibrium with interstitial liquid. Therefore, we investigate the parametric dependence of solute fluxes in the context of convective solutions of the *ideal mushy-layer equations* (Worster 1997, 2000). The applicability of mushy-layer theory to sea ice modelling has been demonstrated by Feltham *et al.* (2006) and reviewed by Hunke *et al.* (2011). However, the theory developed in this paper is more widely applicable, for instance to controlling macrosegregation, which is variation in the composition of a casting of a metal alloy.

Linear stability analysis (Worster 1992*a*) indicates that the dominant dimensionless parameter governing the onset of convection in a mushy layer is a type of Rayleigh number. This parameter relates the available gravitational potential energy (dominated by the interstitial salinity gradient) to the dissipation caused by thermal diffusion and fluid viscosity. A Rayleigh number has been used to interpret the onset of convection in the experiments of Wettlaufer, Worster & Huppert (1997) and the confinement of convection to a lower layer of sea ice (Notz & Worster 2008). Recently, preliminary parameterizations of convection within sea ice that incorporate a Rayleigh number have been developed by Vancoppenolle *et al.* (2010) and by Petrich, Langhorne & Eicken (2011).

The fully developed system with chimneys is not amenable to complete analytical treatment. Therefore, some have used an enthalpy-based approach where a single set of equations applies both to the mushy layer and to the liquid melt. Beckermann & Wang (1995) and Boettinger *et al.* (2002) review the use of this type of technique applied numerically to the casting of metal alloys, and Oertling & Watts (2004) apply this technique to sea ice modelling. Others (Schulze & Worster 1998; Chung & Worster 2002; Wells, Wettlaufer & Orszag 2010) have solved separate equations describing the mushy layer and the liquid melt. The computational complexity of such numerical approaches, even with considerable simplifications, means that they are not readily applicable to predictive sea ice modelling. In sea ice, the spacing of brine channels is of the order of centimetres and so is unresolvable in present-day climate models.

Recently, Wells *et al.* (2010) investigated the dependence of solute flux on chimney spacing and suggested that the spacing takes the value that maximizes the flux. This dynamic *maximum-flux criterion* needs to be tested further but constitutes an objective and transparent way to determine the otherwise unknown chimney spacing.

Here we develop a simple theoretical framework for modelling fluxes though chimneys using an idealized steady-state solidification arrangement described in § 2. This steady-state arrangement corresponds to the experimental set-up described in Peppin *et al.* (2007) but also applies to transient situations in which the evolution of the system is much slower than the convective turnover time. In § 3, we develop a patchwork of simplifying approximations, motivated by the case of high Rayleigh number, that captures the essential physics while rendering the problem analytically tractable. We use a vertically linear temperature profile, which would be a good approximation across a thin convecting layer at the bottom of sea ice. This linear profile allows us to find a similarity solution, reducing the full nonlinear two-dimensional internal convection problem to readily solved ordinary differential equations. In § 4, we investigate the behaviour of the solution for a planar array of chimneys and the dependence of flux on chimney spacing. Then in § 5, we apply the maximum-flux criterion to derive analytically the dependence of heat and solute

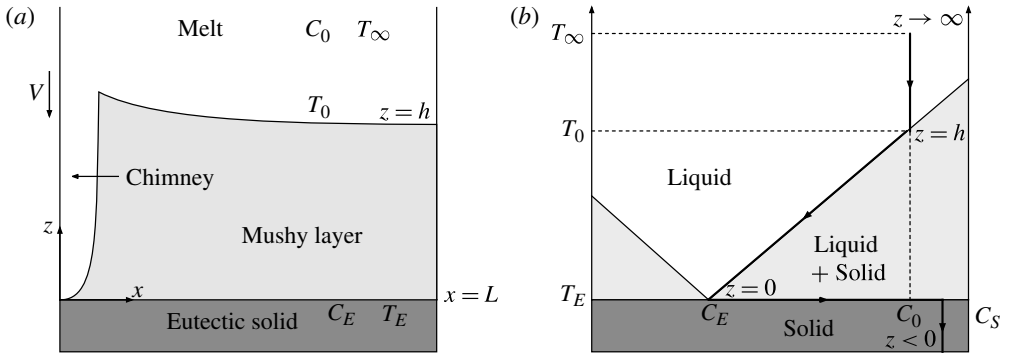

FIGURE 1. (*a*) Diagram of the problem arrangement; and (*b*) the phase diagram showing the phase of the binary alloy as a function of concentration and temperature. The arrows show a trajectory as the system evolves from melt to solid. Note that V is the speed at which the solidification cell is pulled downwards between fixed heat exchangers and equals the rate of solidification.

fluxes on the mush Rayleigh number and on the other dimensionless parameters of the system.

Finally, in § 6, we generalize our model to three dimensions and demonstrate that an array of chimneys can be characterized by the average drainage area alone. We therefore solve the generalization of our model in detail in an axisymmetric geometry and determine the relationship between solute flux, mush Rayleigh number and the other dimensionless parameters.

This work leads us to propose dimensional relationships not only for solute and heat fluxes through chimneys, but also for the vertical structure of the interstitial flow field and solid fraction distribution. These have the potential to be incorporated into a one-dimensional model of sea ice, as discussed in § 7.

2. Problem formulation

We consider convection through a mushy layer and chimney as depicted in figure 1. A solidification cell, containing a binary alloy whose less dense component is preferentially rejected on solidification, is pulled downwards at a constant speed V through fixed heat exchangers. The steady state has a chimney centred on $x = 0$ and chimney half-spacing L, as shown in figure 1(*a*). The lower heat exchanger is held at the eutectic temperature T_E, below which the alloy freezes completely for all solute concentrations. The far field has temperature T_∞ and solute concentration $C_0 > C_E$, where C_E is the eutectic concentration. Let T_0 be the liquidus temperature corresponding to C_0 and let C_S be the concentration of the solid phase. These quantities are shown in figure 1(*b*), which also shows the trajectory through the phase diagram as the system evolves from melt ($z > h$), to mushy layer ($0 < z < h$) and then to solid $z < 0$. The liquidus is assumed to be linear with slope Γ.

Note that this situation is dynamically equivalent to saltwater (with $C_0 < C_E$) in a cell pulled upwards towards a eutectic heat exchanger, since, in the case of saltwater, the more dense component is preferentially rejected on solidification.

2.1. *Governing equations*

For the sake of mathematical transparency, we consider an ideal binary alloy, one whose thermodynamic properties are independent of phase (Worster 1997, 2000). This is governed by the ideal mushy-layer equations. These dimensionless equations, describing conservation of heat, solute, momentum and mass in steady state, are respectively

$$\boldsymbol{u}\cdot\boldsymbol{\nabla}\theta - \frac{\partial\theta}{\partial z} = \nabla^2\theta - \mathscr{S}\frac{\partial\phi}{\partial z}, \tag{2.1}$$

$$\boldsymbol{u}\cdot\boldsymbol{\nabla}\theta - (1-\phi)\frac{\partial\theta}{\partial z} = -(\theta-\mathscr{C})\frac{\partial\phi}{\partial z}, \tag{2.2}$$

$$\boldsymbol{u} = -R_m(\boldsymbol{\nabla}p + \theta\boldsymbol{e}_z), \tag{2.3}$$

$$\boldsymbol{\nabla}\cdot\boldsymbol{u} = 0. \tag{2.4}$$

The mushy layer is a porous medium with solid fraction ϕ and Darcy velocity $\boldsymbol{u}$. $\boldsymbol{e}_z$ denotes a unit vector in the z-direction. The dimensional velocity scale is V and the dimensional length scale is $L_T \equiv \kappa/V$ where κ is the thermal diffusivity. We use a linear equation of state for density $\rho = \rho_0[1+\beta\Delta C\theta]$ and assume constant permeability

$$\Pi = \Pi_0 \tag{2.5}$$

for the sake of analytical tractability. The Stefan number $\mathscr{S} = \mathscr{L}/(c_p\Delta T)$ governs the ratio of latent heat $\mathscr{L}$ release to driving temperature gradient $\Delta T = T_0 - T_E$ and specific heat c_p. The compositional ratio $\mathscr{C} = (C_S - C_E)/\Delta C$, where $\Delta C = C_0 - C_E$. Since the mushy layer is in local thermodynamic equilibrium, we use a single variable

$$\theta = (T - T_E)/\Delta T = (C - C_E)/\Delta C \tag{2.6}$$

to describe both temperature T and interstitial concentration C. This gives $\theta = 0$ at $z = 0$ and $\theta = 1$ at $z = h$.

Since $\boldsymbol{\nabla}\cdot\boldsymbol{u} = 0$, we can introduce a streamfunction ψ and write $\boldsymbol{u} = (-\psi_z, \psi_x)$ in the planar geometry we are considering. Eliminating the pressure in Darcy's law (2.3), we find the vorticity equation

$$\nabla^2\psi = -R_m\theta_x, \tag{2.7}$$

where

$$R_m = \frac{\beta\Delta C g\Pi_0}{\nu V} \tag{2.8}$$

is the mush Rayleigh number, with gravitational acceleration g and kinematic viscosity of the liquid phase ν. This important non-dimensional parameter governs the onset of convection within a mushy layer (Worster 1992*a*) and relates the driving buoyancy difference to the dissipation caused by convection within the mush. The depth of a mushy layer is controlled by thermal diffusion (Huppert & Worster 1985), so this definition of the Rayleigh number is equivalent to standard definitions for convection in a porous medium, which have L_T/κ in place of $1/V$.

We consider the further simplification $\mathscr{C} \gg 1$. In this limit, the equation of salt conservation (2.2) determines the solid fraction ϕ through

$$\mathscr{C}\phi_z = \boldsymbol{u}\cdot\boldsymbol{\nabla}\theta - \theta_z. \tag{2.9}$$

This decouples the thermal equation (2.1) and gives $\Omega\,(\boldsymbol{u}\cdot\boldsymbol{\nabla}\theta-\theta_z)=\nabla^2\theta$, where the parameter $\Omega=1+\mathscr{S}/\mathscr{C}$ is a dimensionless effective specific heat capacity; in particular, Ω is the factor by which the specific heat capacity is enhanced owing to latent heat release (Worster 2000; Huppert & Worster 2012).

Additionally, with the further simplification $R_m\gg 1$, frame advection is negligible compared to Darcy transport. Therefore, we neglect frame advection throughout this paper. In particular, this reduces the decoupled thermal equation to

$$\Omega\boldsymbol{u}\cdot\boldsymbol{\nabla}\theta=\nabla^2\theta. \tag{2.10}$$

2.2. *Boundary conditions*

At the chimney wall ($x=a(z)$), the interstitial liquid flows from the mush into the chimney, so the solid fraction is zero there, and marginal equilibrium and heat conservation are expressed by

$$\boldsymbol{u}\cdot\boldsymbol{\nabla}\theta=0,\quad \theta_x=(\psi-x)\theta_z\quad (x=a), \tag{2.11a,b}$$

as shown by Schulze & Worster (1999). Conservation of mass at the chimney wall can be expressed by

$$\psi=\frac{a^3}{3\mathscr{D}}\left[\psi_x+R_m(\theta-\overline{C})\right]+a\psi_x\quad (x=a), \tag{2.11c}$$

where $\overline{C}$ is the average concentration in the chimney (Chung & Worster 2002). The final term can be neglected if the Darcy number $\mathscr{D}=\Pi_0V^2/\kappa^2\ll 1$. We adopt this simplification, which ensures $a\ll 1$ and so allows us to apply (2.11*a,b*) at $x=0$.

At $x=L$ (the dimensionless chimney half-spacing), we apply symmetry boundary conditions, namely

$$\boldsymbol{u}\cdot\boldsymbol{n}=0\Rightarrow\psi_z=0,\quad \boldsymbol{n}\cdot\boldsymbol{\nabla}\theta=0\Rightarrow\theta_x=0\quad (x=L). \tag{2.12a,b}$$

We also impose zero vertical velocity at the lower boundary with the eutectic solid,

$$\boldsymbol{u}\cdot\boldsymbol{n}=0\Rightarrow\psi_x=0\quad (z=0). \tag{2.13}$$

3. The chimney–active–passive model

We develop a simple model designed to capture the essential dynamics of convection using a patchwork of approximations in different regions (see figure 2) as follows.

Away from the chimney (§ 3.1), we assume a vertically linear and horizontally uniform temperature field. There is no baroclinic torque, since the temperature is horizontally uniform, so this region is essentially 'passive', providing the fluid flux required by the actively convecting near-chimney region.

To determine the strength of this flow, we consider the 'active region' near the chimney (§ 3.2) where convection is driven by baroclinic torque. We find a similarity solution to the mushy-layer equations that also has linear vertical temperature variation, and we patch this to the passive region (§ 3.3).

The flow field in the liquid region is computationally very expensive to find. Therefore we rather balance heat fluxes across a thermal boundary layer to the mush–liquid interface, as suggested by Fowler (1985) and implemented in some numerical studies (Schulze & Worster 1998; Wells *et al.* 2010). This gives us a chimney–active–passive (CAP) model

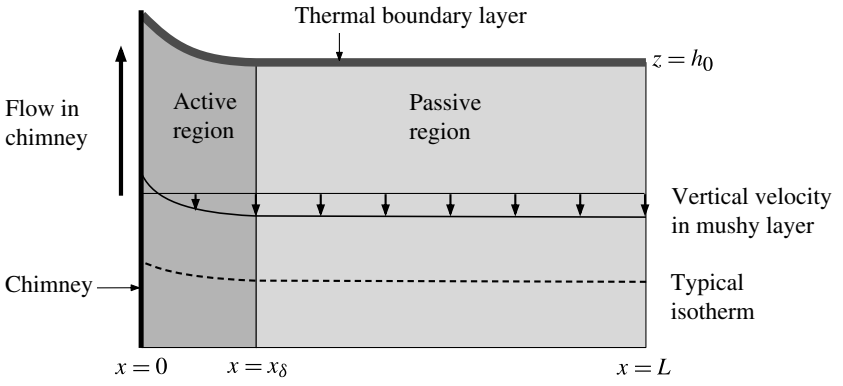

FIGURE 2. The CAP model, showing the active region $x < x_\delta$, passive region $x_\delta < x < L$ and thermal boundary layer to the melt above. The vertical component of the Darcy velocity is uniform and negative in the passive region, and most of the upward flow occurs in the chimney.

3.1. *Passive region: analysis of the bulk mush*

Away from the chimney we assume that the temperature field is directly proportional to z and has no horizontal variation. This automatically satisfies the symmetry boundary condition (2.12*b*). Consistently with this temperature field, we seek a solution for the flow field with horizontally uniform vertical velocity $w = \psi_x$. The streamfunction that satisfies the vorticity equation (2.7) and the boundary conditions (2.12*a*), (2.13) is

$$\psi \propto z(L - x). \tag{3.1}$$

In contrast to previous numerical studies (Schulze & Worster 1998; Chung & Worster 2002; Wells *et al.* 2010), we do not impose a condition of constant pressure at $z = h$.

The passive region has a uniform depth h_0 since there is no horizontal temperature or vertical velocity variation in this region and the mush–liquid interface is at a constant temperature. The depth h_0 is determined by balancing advection and diffusion of heat across a thermal boundary layer at the mush–liquid interface. This gives (Fowler 1985)

$$\boldsymbol{n} \cdot \boldsymbol{\nabla}\theta = -\theta_\infty \boldsymbol{u} \cdot \boldsymbol{n} \quad (z = h_0), \tag{3.2}$$

where $\theta_\infty = (T_\infty - T_0)/(T_0 - T_E)$.

The passive region has a simple structure and flow field, but the strength of this flow must be determined by considering the active region near the chimney.

3.2. *Active region: similarity solution near the chimney*

The reduced mushy-layer equations (2.7) and (2.10),

$$\nabla^2 \psi = -R_m \theta_x, \quad \Omega \boldsymbol{u} \cdot \boldsymbol{\nabla}\theta = \nabla^2 \theta, \tag{3.3}$$

admit a similarity solution

$$\psi = z\left(\frac{R_m}{\Omega h_0}\right)^{1/2} \Psi(\eta), \quad \theta = \frac{z}{h_0}\Theta(\eta), \quad \eta = x\left(\frac{R_m \Omega}{h_0}\right)^{1/2}, \tag{3.4}$$

that has the same vertical structure as the passive region. The mush–liquid interface is at $z = h(x) = h_0/\Theta(\eta)$.

3.2.1. *Similarity equations and boundary conditions*

In terms of the similarity variables (3.4), the reduced mushy-layer equations (3.3) give similarity equations

$$\Theta'' = -\Psi\Theta' + \Psi'\Theta, \quad \Psi'' = -\Theta', \tag{3.5a,b}$$

and the boundary conditions (2.11*a,b*) of marginal equilibrium and heat conservation give

$$\Psi'\Theta = \Psi\Theta', \quad \Theta' = \Psi\Theta/\Omega \quad (\eta = 0). \tag{3.6a,b}$$

These can be combined to show that the vertical velocity Ψ' is always positive at the chimney wall.

3.2.2. *Finding the chimney width*

To apply mass conservation (2.11*c*) at the mush–chimney boundary ($x = a$), we determine the average concentration in the chimney in terms of our similarity variables. We neglect solute diffusion in the chimney, so $\boldsymbol{u}\cdot\nabla C = 0$ and $C = C(\psi)$ only. Following Chung & Worster (2002), we use the approximation

$$\overline{C}(z) = \frac{1}{\psi(a(z), z)}\int_0^{\psi(a(z),z)} C(\psi)\,\mathrm{d}\psi, \tag{3.7}$$

which gives $\overline{C}(z) = (z/2h_0)\Theta_0$ in our similarity variables, and we use the notation $\Theta_0 \equiv \Theta(0)$. Then (2.11*c*) implies that

$$a \sim \mathscr{D}^{1/3}R_m^{-1/6}\Omega^{-1/6}h_0^{1/6}\alpha, \quad \text{where } \alpha = \left[3\Psi_0/(\Psi_0' + \Theta_0/2)\right]^{1/3}. \tag{3.8}$$

It is important to note that the chimney width a is independent of z, so chimneys are predicted to be straight-sided. Previously unpublished work by Ashmore & Worster (see Appendix) considers power-law background temperature profiles $\theta \sim z^b$ and shows that $a \sim z^{(1-b)/6}$. Therefore a straight-sided chimney is a consequence of the linear temperature profile we imposed in the passive region. Although our prediction of straight-sided chimneys is a consequence of this linear profile, it is somewhat encouraging to note that this corresponds to some experimental results, such as those of Schulze & Worster (1998), reproduced in figure 3.

3.3. *Patching conditions*

It is not appropriate to match the active and passive regions asymptotically in our simple model. Instead, we patch them at a position $x = x_\delta$ (shown in figure 2) that is internally determined by applying conditions of continuity of temperature, normal heat flux, normal velocity and pressure there.

Let $\delta = x_\delta(R_m\Omega/h_0)^{1/2}$. Continuity of temperature and normal heat flux require that

$$\Theta(\delta) = 1, \quad \Theta'(\delta) = 0. \tag{3.9a,b}$$

Then continuity of normal velocity determines the strength of convection in the passive region, so (3.1) for the streamfunction in the passive region becomes

$$\psi = z\left(\frac{R_m}{\Omega h_0}\right)^{1/2}\Psi(\delta)\left[\frac{L-x}{L-x_\delta}\right]. \tag{3.10}$$

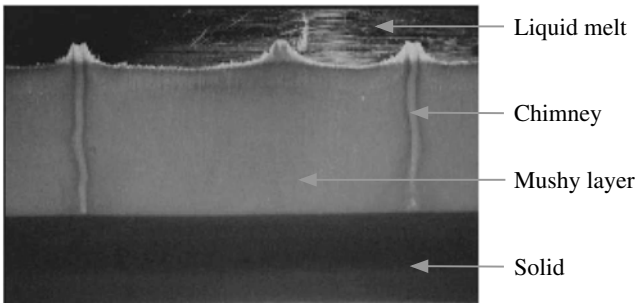

FIGURE 3. From Schulze & Worster (1998). Photograph of an ammonium-chloride solidification experiment, showing narrow vertical chimneys. Note that the mush–liquid interface is peaked near the chimneys and flat in the 'passive zone' further away, which corresponds to our model, shown in figure 2.

Applying continuity of pressure, by integrating the vertical component of (2.3), allows us to determine x_δ through

$$L = (R_m \Omega / h_0)^{-1/2} F(\delta, \Omega)^{-1}, \quad \text{where } F(\delta, \Omega) \equiv \left(\delta - \Psi(\delta)/\Psi'(\delta)\right)^{-1}. \tag{3.11}$$

Note that $F(\delta, \Omega)$ is an implicit function of Ω, since Ω affects the active-region boundary conditions (3.6). Then (3.2) determines the depth of the layer

$$h_0 = \left(-\theta_\infty R_m \Psi'(\delta)\right)^{-1}. \tag{3.12}$$

Substituting this equation back into (3.11), we find

$$L = R_m^{-1} \theta_\infty^{-1/2} G(\delta, \Omega), \quad \text{where } G(\delta, \Omega) = F(\delta, \Omega)^{-1} \left(-\Omega \Psi'(\delta)\right)^{-1/2}. \tag{3.13}$$

3.4. *Determining solute and heat fluxes*

The flux of salt from the mushy layer to the liquid is equal to the total advective flux of salt into the chimney, which is determined from the solution of the active region. Each half-chimney drains a region of mush of length L. Therefore, the average flux of solute per unit length in the x-direction is

$$\mathscr{F}_{Solute} = \frac{1}{L} \int_0^h \left[\psi_z(\theta - 1)\right]_{x=0} \mathrm{d}z = -\frac{1}{2} R_m \frac{\Psi_0}{\Theta_0} F(\delta, \Omega). \tag{3.14}$$

Note that the solute flux is negative because it is solute-depleted fluid that emanates from the chimney (cf. figure 1*b*).

The dimensional temperature at the top of the chimney is T_0 and by symmetry ψ vanishes at the centre of the chimney. Therefore the additional heat flux per unit length, due to convection through chimneys, is

$$\mathscr{F}_{Heat} = \frac{1}{L} \int_0^a \left[\psi_x \theta_\infty\right]_{z=h} \mathrm{d}x = -\theta_\infty R_m \frac{\Psi_0}{\Theta_0} F(\delta, \Omega). \tag{3.15}$$

Note that $\mathscr{F}_{Heat}$ is negative because the far-field temperature is greater than the temperature at the interface.

These relations can be simply expressed (still dimensionlessly) by

$$\mathscr{F}_{Solute} = -R_m \gamma(\delta, \Omega), \tag{3.16}$$

$$\mathscr{F}_{Heat} = -2\theta_\infty R_m \gamma(\delta, \Omega), \tag{3.17}$$

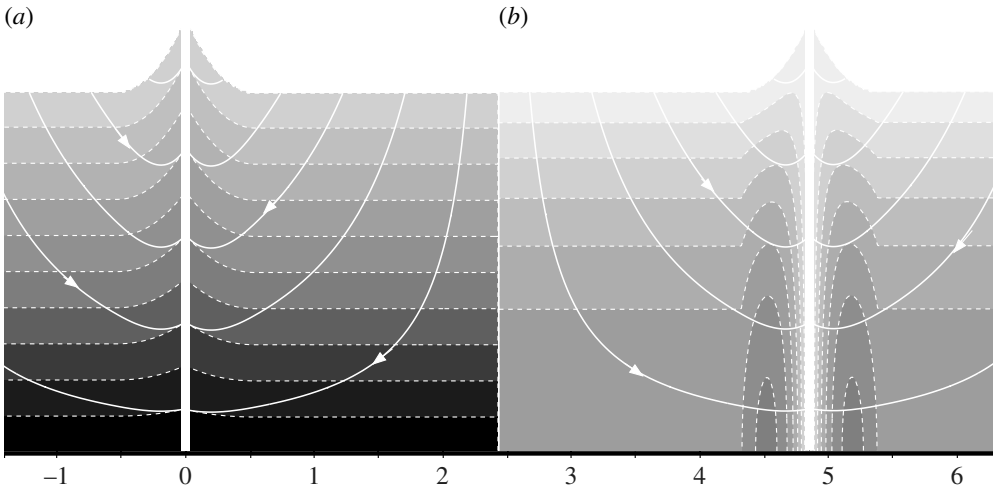

FIGURE 4. A typical solution of the CAP model, showing part of a periodic array of chimneys. Solid white streamlines have arrows that indicate the flow direction. Isotherms in steps of 0.1 (*a*) and contours of solid fraction in steps of 0.005 (*b*) are shown by dashed white curves. The latter start at $\phi = 0$ at the mush–liquid interface. For these parameters ($R_m = 12$, $\theta_\infty = 0.4$, $\Omega = 3.5$ and $\mathscr{C} = 15$, $L = 2.426$), the active region occupies about 22% of the domain. The vertical and horizontal scales are the same, and the chimney width is formally zero as the Darcy number $\mathscr{D} \to 0$, but is shown indicatively.

where

$$\gamma(\delta, \Omega) = \frac{1}{2}\frac{\Psi_0(\delta, \Omega)}{\Theta_0(\delta, \Omega)} F(\delta, \Omega). \tag{3.18}$$

3.5. *Solving the boundary-value problem*

The similarity equations (3.5) and boundary conditions (3.6), (3.9) and (3.11) constitute a boundary-value problem for the active region, which we solve using a fourth-order Runge–Kutta routine and a Newton–Raphson algorithm to update initial guesses for Ψ_0, Θ_0 and δ. The online supplementary material (§ S1.2) available at journals.cambridge.org/flm considers both the existence and uniqueness of solutions to this boundary-value problem. As discussed there, we restrict attention to solutions that have only one turning point $\Psi' = 0$ as these correspond to upwelling near the chimney and downwelling everywhere else, which is required for consistency with our formulation of the CAP model. This restriction is also consistent with the maximum-flux criterion discussed in § 5.

4. Results of the model

4.1. *Discussion of results*

The general form of the solution in the reduced CAP model is shown in figure 4. It is encouraging to note the similarity with some experiments, such as in figure 3, especially in terms of the shape of the mush–liquid interface. We find qualitative agreement with numerical results obtained by Chung & Worster (2002) and Wells *et al.* (2010). Our model reproduces the trend and main features of the dependence of solute

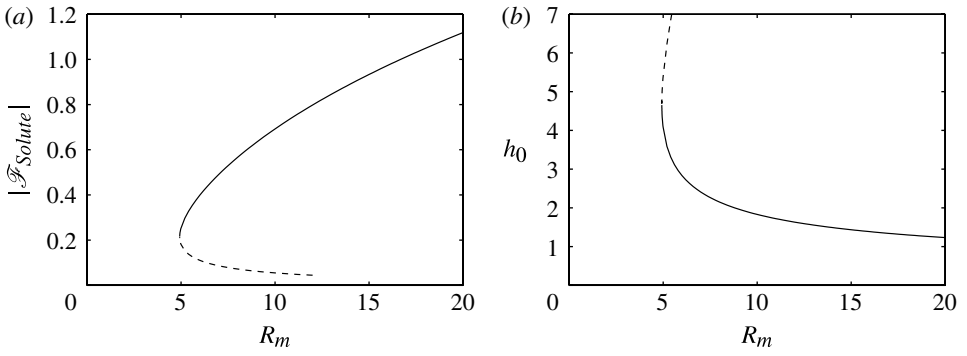

FIGURE 5. (*a*) Dependence of solute flux $\mathscr{F}_{Solute}$ and (*b*) depth of mush h_0 on Rayleigh number R_m at fixed $L = 2.16$, $\Omega = 1.33$, $\theta_\infty = 0.4$. It is believed that the dashed portions are unstable on the basis of the numerical work of Chung & Worster (2002).

flux and depth of the mushy layer found numerically. For example, figure 5(*a,b*) can be compared with figure 5(*b,c*) in Chung & Worster (2002).

However, this highly simplified model does not yield quantitative agreement with the results of Chung & Worster (2002). For instance, comparing the above figures, our model consistently predicts higher solute fluxes. It is not appropriate to undertake a full comparison because Chung & Worster (2002) use relatively high Darcy numbers and quite moderate Rayleigh numbers, a parameter regime in which we do not expect agreement, even before the differing assumptions. Instead, we identify the main causes of discrepancy.

First, we deliberately chose to neglect frame advection in order to render the problem analytically tractable by similarity solution in the active region. However, it is certainly quantitatively important at low to moderate Rayleigh numbers and results in temperature profiles closer to the exponential profiles derived theoretically in the case of no convection (Hills, Loper & Roberts 1983; Worster 1991) than the linear profile we have assumed. Connected with this, we did not impose a constant pressure at $z = h$, unlike Chung & Worster (2002), which means that the horizontal velocity was not zero there and consequently the flow field has a slightly different shape.

Secondly, we decoupled the heat equation from the salt conservation equation through the effective specific heat capacity Ω and so have neglected the feedback on permeability which we assumed constant.

4.2. *Dependence on chimney spacing*

The flux of solute and heat through a chimney depends on the size of the convecting cell. Increasing the chimney spacing increases the width of the active region, sustaining a larger flow driven by a greater temperature difference. Therefore the flux into an individual chimney is increased. However, while the average flux per unit length in the x-direction initially increases (above a minimum chimney spacing required to sustain flow), it eventually decreases. There is therefore a maximum flux at some moderate chimney spacing (see figure 6). In their numerical study, Wells *et al.* (2010) observed the existence of such maxima.

Note that for a fixed chimney spacing there is a critical Rayleigh number required to sustain convection as shown in figure 5(*a*) and observed previously (Schulze & Worster 1998; Chung & Worster 2002; Wells *et al.* 2010). However, in contrast to their

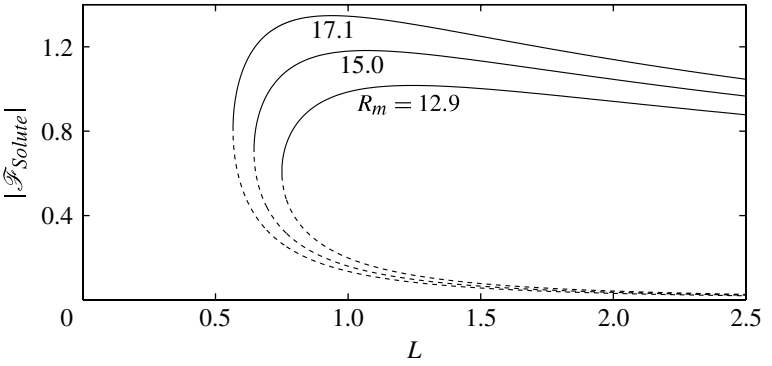

FIGURE 6. The dependence of solute flux on chimney spacing at three different values of R_m. Other parameters are as in figure 5. There is a well-defined local maximum whose position moves to lower chimney spacing as R_m increases.

findings, as L is increased, this critical Rayleigh number continues to decrease to 0. Therefore, at every Rayleigh number, a sufficiently large box could sustain convection, and we find no overall critical Rayleigh number. This discrepancy is likely to be caused by our neglect of frame advection, which dominates at low Rayleigh number.

5. Maximum-flux criterion

Thus far we have imposed the chimney half-spacing L; but this is undetermined *a priori*. Therefore, we employ the maximum-flux criterion suggested by Wells *et al.* (2010) that L takes the value that maximizes the solute flux from the mushy layer. This approach certainly allows us to compute an upper bound on the solute flux and importantly avoids artificially imposing a horizontal length scale.

As shown in figure 6, the flux is a well-defined function of chimney spacing on each branch of solutions. Therefore, we combine (3.16) for the flux with (3.13) for the chimney spacing to find that

$$\left.\frac{\partial \mathscr{F}_{Solute}}{\partial L}\right|_{R_m,\theta_\infty,\Omega} = -R_m^2\theta_\infty^{1/2}\left(\left.\frac{\partial G}{\partial \delta}\right|_{\Omega}\right)^{-1}\left.\frac{\partial \gamma}{\partial \delta}\right|_{\Omega}. \tag{5.1}$$

As illustrated in figure 7(*a*) and discussed further in the supplementary material, § S2, $G(\delta, \Omega)$ is a well-defined function of δ, and $\partial G/\partial\delta$ is strictly positive on the upper branch and strictly negative on the lower branch. Therefore

$$\left.\frac{\partial \mathscr{F}_{Solute}}{\partial L}\right|_{R_m,\theta_\infty,\Omega} = 0 \quad \Leftrightarrow \quad \left.\frac{\partial \gamma}{\partial \delta}\right|_{\Omega} = 0. \tag{5.2}$$

5.1. *Solute fluxes under the maximum-flux criterion*

Figure 7(*b*) illustrates the existence of a unique maximum value of $\gamma(\delta, \Omega)$, which we denote $\gamma_c(\Omega)$. In the case $\Omega \to \infty$, we prove the uniqueness of the maximum in the supplementary material, § S3. We can determine $\gamma_c(\Omega)$ once and for all by solving the active-region equations independently of all the other external parameters. Therefore, if the maximum-flux criterion holds, (3.16) and (3.17) imply that

$$\mathscr{F}_{Solute} = -R_m\gamma_c(\Omega), \tag{5.3}$$

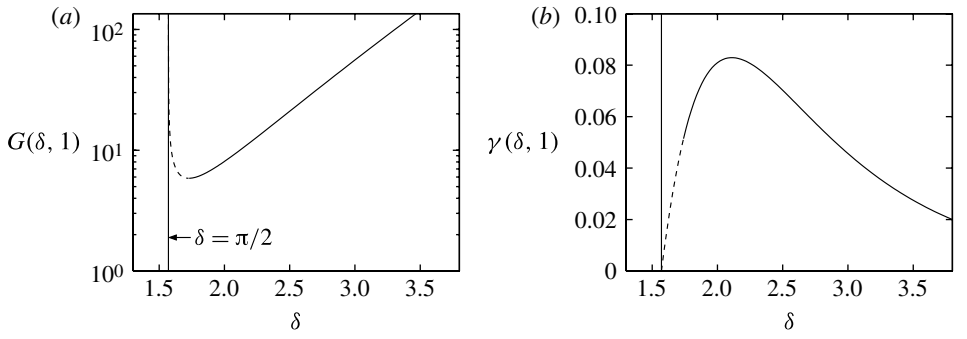

FIGURE 7. (*a*) $G(\delta, \Omega = 1)$, which is proportional to the chimney spacing. The global minimum corresponds to the minimum chimney spacing required to sustain convection. Above this, the two solutions to $G(\delta, \Omega) = G_0$ constant correspond to the two branches in figures 5 and 6, denoted by the dashed and solid curves. (*b*) $\gamma(\delta, \Omega = 1)$, which is proportional to the solute flux. Below the line $\delta = \pi/2$ there are no solutions of the boundary-value problem, indicating that there must be a finite active region where baroclinic torque occurs in order to drive convection. These results are derived in the supplementary material, § S2.2.

$$\mathscr{F}_{Heat} = -2\theta_\infty R_m \gamma_c(\Omega). \tag{5.4}$$

An approximately linear relationship between solute flux and Rayleigh number has also been found using direct numerical simulation of the mushy-layer equations under the maximum-flux criterion (Wells *et al.* 2010), although they found a cut-off at low R_m. At sufficiently high R_m, this difference can be neglected, and so our analytic derivation of this relationship under simplifying approximations provides additional assurance of the robustness of their numerical observation obtained by testing across a subset of parameter space.

Additionally, our model, combined with the maximum-flux criterion, reduces the parametric dependence by showing that the flux is independent of far-field temperature θ_∞. Importantly, we have also shown that while the width of the chimney $a \to 0$ in the limit of small Darcy number $\mathscr{D} \to 0$ (cf. equation (5.10) below), the flux tends to a constant value. Therefore, to leading order, the flux depends only on the Rayleigh number and the effective specific heat capacity Ω.

5.2. *Dependence on* Ω

The coefficient $\gamma_c(\Omega)$ in (5.3) and (5.4) decreases with Ω, as shown in figure 8(*a*). A high value of Ω, which corresponds to high dimensional effective specific heat capacity $c_p\Omega$, reduces the strength of convection within the mush and so reduces solute flux. Mathematically, this is as we expect from the boundary conditions (3.6*a*,*b*) which imply that the strength of convection scales with Ω^{-1}, a result that we prove in the supplementary material, § S3.

However, linear stability analysis shows that the onset of convection is set by $\Omega R_m = (\Omega R_m)_{crit.}$ (Lapwood 1948; Huppert & Worster 2012). Therefore, large Ω makes convection more likely but decreases the resulting solute flux (figure 8*b*).

5.3. *Vertical transport, solid fraction and length scales*

In addition to determining the solute and heat fluxes through chimneys, our model also determines the interstitial velocity within the mushy layer. In particular, we

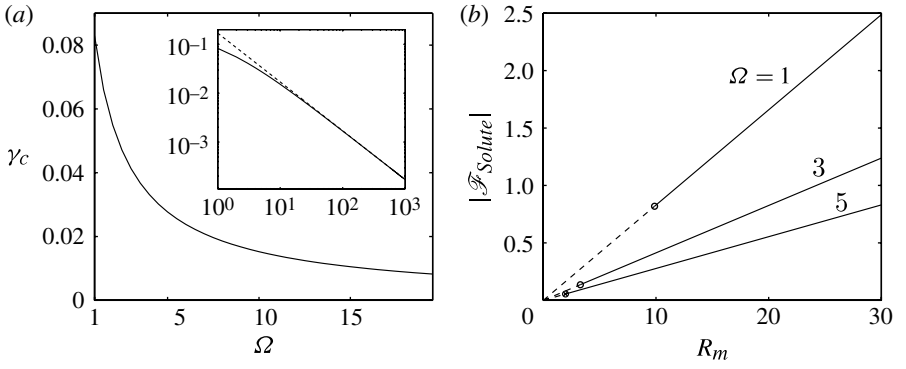

FIGURE 8. (*a*) The coefficient $\gamma_c(\Omega)$ in the expression for the maximum flux (5.3). Inset shows a log–log plot with the dashed asymptotic result $\gamma_c \sim \Omega^{-1}$, derived in the supplementary material, see equation (S3.21). (*b*) The relationship between solute flux and Rayleigh number with a cut-off indicated by o, determined from the condition $\Omega R_m = (\Omega R_m)_{crit.} = \pi^2$ (Huppert & Worster 2012). Below this, a dashed curve indicates our model results.

find that the vertical component w, which controls vertical salt transport within the ice matrix, is

$$w = \begin{cases} -R_m(z/h_0)\left[-\Psi'(\delta)\right] & \text{passive region } x \geqslant x_\delta, \\ -R_m(z/h_0)\left[-\Psi'(\eta(x))\right] & \text{active region } x \leqslant x_\delta. \end{cases} \tag{5.5}$$

Therefore, the vertical velocity w is proportional to the distance from the eutectic solid and proportional to the Rayleigh number. In the passive region w is independent of x and, since under the maximum-flux criterion $\Psi'(\delta)$ depends only on Ω, we can write

$$w = -R_m(z/h_0)w_c(\Omega) \quad \text{where} \quad w_c(\Omega) = -\Psi'(\delta) > 0. \tag{5.6}$$

To determine the solid fraction ϕ, we integrate (2.9), neglecting frame advection, and find that

$$\phi = \begin{cases} w_c(\Omega)\,(R_m/2\mathscr{C})\left[1-(z/h_0)^2\right] & \text{passive region } x \geqslant x_\delta, \\ -\Theta''(\eta(x))\,(R_m/2\mathscr{C})\left[\Theta\,(\eta(x))^{-2}-(z/h_0)^2\right] & \text{active region } x \leqslant x_\delta. \end{cases} \tag{5.7}$$

These are equal at the patching boundary x_δ and satisfy the boundary condition $\phi = 0$ at the mush–liquid interface $z = h$. The vertical structure of the solid fraction is therefore quadratic, and contours of ϕ, as well as streamlines, are shown in figure 4.

In summary, scalings for the depth of the mush (from (3.12)), chimney spacing (from (3.13)), and chimney width (from (3.8)) are

$$h_0 = R_m^{-1}\theta_\infty^{-1}h_c(\Omega), \tag{5.8}$$

$$L = R_m^{-1}\theta_\infty^{-1/2}L_c(\Omega), \tag{5.9}$$

$$a = R_m^{-1/3}\mathscr{D}^{1/3}\theta_\infty^{-1/6}a_c(\Omega). \tag{5.10}$$

The chimney width a is only weakly dependent on Ω (figure 9*b*,*c*). Furthermore, a is independent of the permeability, since both R_m and $\mathscr{D}$ are proportional to Π_0. This is significant because it is often hard to determine Π_0 precisely. The $\mathscr{D}^{1/3}$ scaling for chimney width a corresponds to the scaling of Schulze & Worster (1998) (and verified

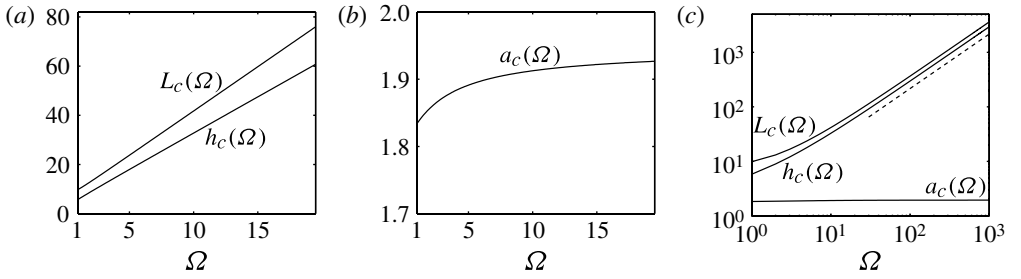

FIGURE 9. (*a*) The dependence of the horizontal and vertical length scales on Ω. (*b*) The weak dependence of chimney width on Ω. These are shown for a larger range of Ω in (*c*). The dashed line has slope 1, and both L_c, $h_c \sim \Omega$. The aspect ratio $L_c/h_c \to 1.23$.

numerically by Chung & Worster 2002), although the former paper proposes $a \sim R_m^{-2/9}$. This difference occurs because we have used the maximum-flux criterion to determine the overall horizontal length scale, rather than imposing the chimney spacing.

Figure 9(*a*,*c*) shows that h_c and L_c depend approximately linearly on Ω. This means that the aspect ratio of the convecting cell $L/h_0 \sim \theta_\infty^{1/2}$, and suggests that the convecting cell has aspect ratio of order unity under the maximum-flux criterion. Order-unity aspect ratios are often observed in experiments (see figure 3 for example).

6. Extension of the model to three dimensions

Mushy layers usually form in non-planar geometries, so it is important to consider potential three-dimensional effects. The whole dynamics of the planar solution is driven by the structure of the active region near the chimney. This suggests that we can reasonably generalize to a three-dimensional mushy layer with distributed chimneys by finding an axisymmetric solution near the chimney and then patching onto an arbitrary passive region. The generalized CAP model is shown in figure 10.

In § 6.1, we consider an entirely axisymmetric problem in a domain bounded by an outer cylinder of radius R, directly extending the CAP model developed in § 3 for a planar geometry. Then in § 6.2, we investigate whether and how this can applied to a non-axisymmetric drainage area. Finally, in § 6.3, we present results in the axisymmetric geometry.

6.1. *Axisymmetric chimney, active and passive zones*

The axisymmetric versions of the heat conservation (2.10) and the vorticity equations (2.7) are

$$\Omega(-\psi_z\theta_r + \psi_r\theta_z) = (r\theta_r)_r + r\theta_{zz}, \quad (\psi_r/r)_r + \psi_{zz}/r = -R_m\theta_r, \tag{6.1a,b}$$

where ψ now denotes the Stokes streamfunction such that $\boldsymbol{u} = (-\psi_z/r)\boldsymbol{e}_r + (\psi_r/r)\boldsymbol{e}_z$. The axisymmetric counterparts to the conditions of marginal equilibrium, heat conservation and mass conservation at the chimney boundary (2.11) are expressed by

$$\psi_r\theta_z = \psi_z\theta_r, \quad \theta_r = \frac{\psi\theta_z}{r}, \quad \psi = \frac{a^4}{16\mathscr{D}}\left(\frac{\psi_r}{r} + R_m(\theta - \overline{C})\right) + \frac{a^2}{2}\frac{\psi_r}{r} \quad (r = a). \tag{6.2a,b,c}$$

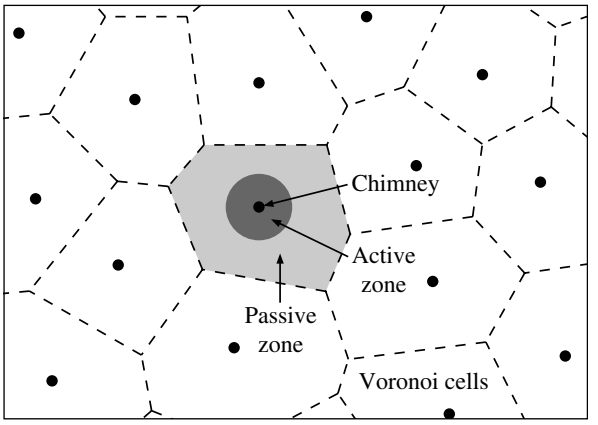

FIGURE 10. Drainage cells (Voronoi cells) in a three-dimensional section of mush, showing the chimneys (black), an active zone (dark grey) and a passive zone (light grey).

6.1.1. *Similarity solution for the active region*

Appropriate scalings for the active region near the chimney are

$$\psi = z\frac{1}{\Omega}\Psi(\eta), \quad \theta = \frac{z}{h_0}\Theta(\eta), \quad \eta = r\left(\frac{R_m\Omega}{h_0}\right)^{1/2}, \tag{6.3}$$

where h_0 is the constant depth of the mushy layer in the passive region. This depth is determined by a balance of the heat fluxes across the thermal boundary layer in the liquid melt, as in the planar geometry, and satisfies

$$h_0 = (\theta_\infty R_m w_e)^{-1}, \quad \text{where } w_e = -\Psi'(\delta)/\delta \tag{6.4}$$

is the negative vertical velocity into the passive region. Substituting the similarity variables into the governing equation (6.1), we obtain

$$-\Psi\Theta' + \Psi'\Theta = (\eta\Theta')', \quad \left(\Psi'/\eta\right)' = -\Theta'. \tag{6.5a,b}$$

We employ the same techniques as in the planar geometry to show $\overline{C} = (z/2h_0)\Theta(\alpha)$. The boundary conditions at the chimney wall (6.2) then become

$$\Psi'\Theta = \Psi\Theta', \quad \Theta' = \frac{\Psi\Theta}{\eta\Omega}, \quad \Psi = \frac{\alpha^4}{16E\Omega w_e}\left(\frac{\Psi'}{\eta} + \frac{\Theta}{2}\right) + \frac{\alpha^2}{2}\frac{\Psi'}{\eta} \quad (\eta = \alpha), \tag{6.6a,b,c}$$

where $\alpha \equiv a(R_m\Omega/h_0)^{1/2}$. The solution of the active region only depends on the dimensionless groups Ω and E, where

$$E = R_m^2\mathscr{D}\theta_\infty. \tag{6.7}$$

Note that, unlike in the planar geometry, the limit $\mathscr{D} \to 0$ can no longer be taken non-singularly because of the geometric constriction of the flow discussed in § 6.3.2. Therefore we retain (6.6*c*) and use this additional boundary condition to determine the free boundary α.

6.1.2. *Passive region and patching conditions*

The passive region is analogous to that in the planar geometry. We apply the conditions $\boldsymbol{u}\cdot\boldsymbol{n} = \boldsymbol{n}\cdot\nabla\theta = 0$ at an outer cylinder $r = R$ and assume a linear thermal field $\theta = z/h_0$. Then by the vorticity equation (6.1*b*) the Stokes streamfunction which corresponds to horizontally uniform vertical velocity is $\psi \propto z(R^2 - r^2)$.

We apply the same four physical conditions as in the planar case to derive patching conditions at radius $r = r_\delta$. The thermal patching conditions are

$$\Theta(\delta) = 1, \quad \Theta'(\delta) = 0, \tag{6.8a,b}$$

where $\delta = r_\delta(R_m\Omega/h_0)^{1/2}$. Then continuity of normal mass flux, which is equivalent to $[\psi_z/r] = 0$, implies that the Stokes streamfunction in the passive region is

$$\psi = z\frac{1}{\Omega}\Psi(\delta)\frac{R^2 - r^2}{R^2 - r_\delta^2} \quad (r_\delta \leqslant r \leqslant R). \tag{6.9}$$

Finally, continuity of pressure, which can be shown to be equivalent to $[\psi_r/r] = 0$, implies

$$R^2 = R_m^{-2}\theta_\infty^{-1}\Omega^{-1}w_e^{-1}\left(\delta^2 - 2\delta\Psi(\delta)/\Psi'(\delta)\right). \tag{6.10}$$

6.2. *An approximate solution in an arbitrary geometry*

Consider an axisymmetric active region of radius r_δ inside a general passive region. The pressure field that drives the flow in the active region corresponding to the similarity solution determined above is

$$p = \frac{1}{\Omega R_m}\int_\delta^\eta \frac{\Psi(\eta')}{\eta'}\,\mathrm{d}\eta' - \frac{z^2}{2h_0}\left(\frac{\Psi'(\delta)}{\delta} + 1\right). \tag{6.11}$$

In the passive region, we assume a linear temperature profile $\theta = z/h_0$ and then solve Darcy's law (2.3) for the flow. Taking the divergence of Darcy's law, we find

$$\nabla^2 p = -\theta_z \equiv -1/h_0, \tag{6.12}$$

where the right-hand side is constant. We seek a separable solution $p = m(x, y) + n(z)$. Let $n''(z) = n_0$, $\nabla^2 m(x, y) = -m_0$, where m_0 and n_0 are constants satisfying $m_0 = n_0 + 1/h_0$. Note that $n = (z^2/2)n_0$, since $w = 0$ at $z = 0$.

To patch the solutions, we impose $[p] = 0$ and $[\boldsymbol{u}\cdot\boldsymbol{n}] = 0$ on $x^2 + y^2 = r_\delta^2$. First, $[p] = 0$ implies that $m = 0$ on $x^2 + y^2 = r_\delta^2$ and

$$n_0 = -\frac{1}{h_0}\left(\frac{\Psi'(\delta)}{\delta} + 1\right), \quad m_0 = -\frac{1}{h_0}\left(\frac{\Psi'(\delta)}{\delta}\right). \tag{6.13a,b}$$

Secondly, $[\boldsymbol{u}\cdot\boldsymbol{n}] = 0 \Rightarrow [\partial p/\partial r] = 0$. Therefore

$$\left.\frac{\partial m}{\partial r}\right|_{x^2+y^2=r_\delta^2} = (R_m\Omega h_0)^{-1/2}\frac{\Psi(\delta)}{\delta}. \tag{6.14}$$

Integrating $\nabla^2 m(x, y) = -m_0$ over the passive region using the divergence theorem, and applying the boundary condition $[\boldsymbol{u}\cdot\boldsymbol{n}] = 0 \Rightarrow [\partial m/\partial r] = 0$ on the outer boundary, we find

$$\left\langle \left.\frac{\partial m}{\partial r}\right|_{x^2+y^2=r_\delta^2} \right\rangle (2\pi r_\delta) = m_0 A_p, \tag{6.15}$$

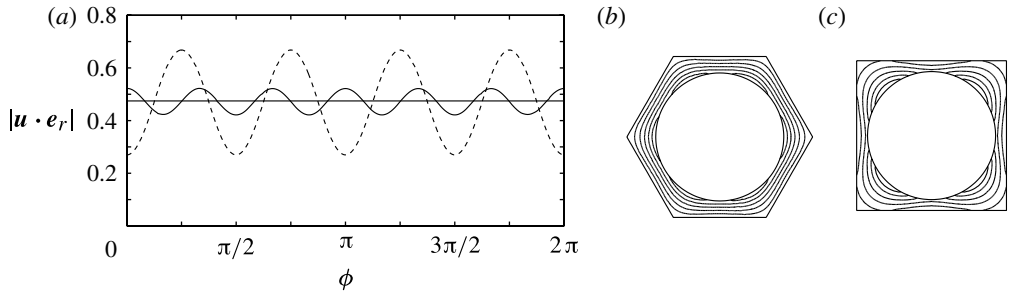

FIGURE 11. Example of the effect of the geometry of the chimney arrangement. (*a*) Computed radial inflow $|\boldsymbol{u}\cdot\boldsymbol{e}_r|$ for a square (– –) and hexagonal (——) array of chimneys as a function of azimuthal angle ϕ in comparison to an axisymmetric passive region (the solid horizontal line). Corresponding contours of $|\nabla m(x,y)|$ in the passive region are shown in (*b*) for hexagonal and (*c*) for square arrays. In this example, $R_m = 20$, $\Omega = 4/3$, $\mathscr{D} = 10^{-4}$ and $\theta_\infty = 1.4$, with outer cylinder radius $R = 0.746$, which maximizes the solute flux through the chimney. For these parameters, the azimuthal variation is about 40 % for the square array, and 10 % for the hexagonal.

where $\langle\cdot\rangle$ denotes the azimuthal average and A_p is the area of the passive region. We substitute (6.15) into (6.14) to obtain the final patching condition. Note that if the passive region is axisymmetric then $A_p = \pi(R^2 - r_\delta^2)$ and we recover the patching condition (6.10) obtained previously.

In non-axisymmetric geometries, we can determine the extent of azimuthal variation by finding $m(x,y)$ numerically using a finite-element method (we used a standard MATLAB package). Two examples presented in figure 11 – square and hexagonal arrays of chimneys with the same total area drained – illustrate the main results. Generically, there is greater azimuthal variation for a square array than a hexagonal array, in which case the variation is usually minimal.

In conclusion, we can approximate a drainage cell of total area A by an axisymmetric region with outer cylinder radius R satisfying

$$R = \left(\frac{A}{\pi}\right)^{1/2}. \tag{6.16}$$

All the patching conditions are satisfied exactly, except $[\boldsymbol{u}\cdot\boldsymbol{n}] = 0$ which is satisfied only in an azimuthally averaged sense, so that mass is conserved globally.

6.3. *Results of the model in the axisymmetric geometry*

6.3.1. *Calculating heat and brine fluxes*

Having shown that a general drainage cell can be modelled using an axisymmetric cell of the same area, we repeat the analysis of § 3.4 in axisymmetry to find the fluxes

$$\mathscr{F}_{Solute} = -R_m\gamma, \tag{6.17}$$

$$\mathscr{F}_{Heat} = -2\theta_\infty R_m\gamma, \tag{6.18}$$

where the multiplying factor,

$$\gamma = \frac{\Psi(\alpha)}{\Theta(\alpha)}\left[\delta^2 - 2\delta\Psi(\delta)/\Psi'(\delta)\right]^{-1} \tag{6.19}$$

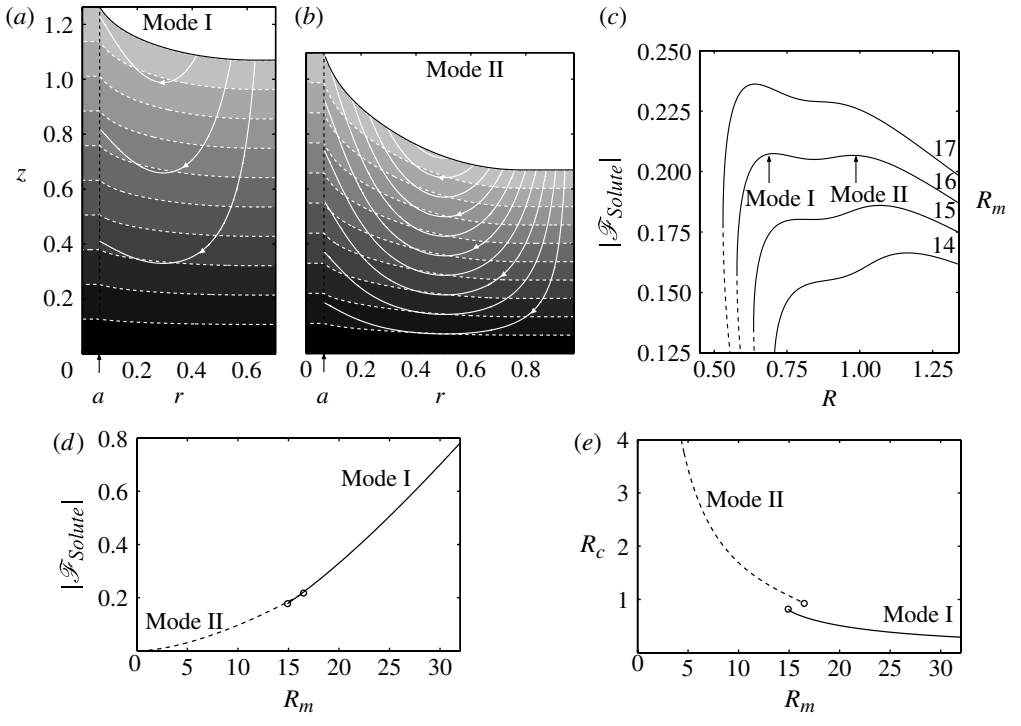

FIGURE 12. (*a*, *b*) The two modes of convection (I, II) for parameters $R_m = 16$, $\theta_\infty = 1.4$, $\mathscr{D} = 1 \times 10^{-4}$ and $\Omega = 1$. Isotherms (dashed white curves), streamlines of Darcy velocity (solid white curves) and the chimney radii at $r = a$ are shown. (*c*) Solute flux against drainage cell radius R, and the change in which local maximum (mode) has the greater flux as we increase R_m from 14 to 17; the dashed curves are lower branches of solutions, analogous to those in figure 6. The transition between modes is shown in (*d*,*e*) with open circles indicating the value of R_m where is there is no longer a local maximum in solute flux corresponding to the mode. (*d*) The maximum value of solute flux and (*e*) the drainage cell radius $R = R_c$ at which the flux is maximized. At higher values of Ω, the transition is rapid, but no longer discontinuous in R_c.

can be found by solving the similarity equations for the active region. The size of the active region δ depends on the external parameters, through the radius of the outer cylinder R, under (6.10).

6.3.2. *Dependence on drainage area and geometric constriction of convection*

In axisymmetry there are additional geometric factors that complicate the dependence of flux on drainage area. In particular, mass conservation $\nabla \cdot \boldsymbol{u} = 0$ means that in the axisymmetric geometry, unlike the planar geometry, the flow is constricted as $r \to a^+$.

Flow constriction gives rise to two distinct modes of convection at certain parameter values. Mode I (figure 12*a*) has a relatively small drainage area and weaker flow. Mode II (figure 12*b*) has a relatively large drainage area which supports a bigger temperature contrast and hence greater flow rates but similar solute fluxes per unit area drained. As R_m increases, the strength of convection increases, which leads to geometric constriction becoming more significant. This inhibits mode II relative to mode I (figure 12*c*, *e*). This complicating detail has a minimal effect on the solute

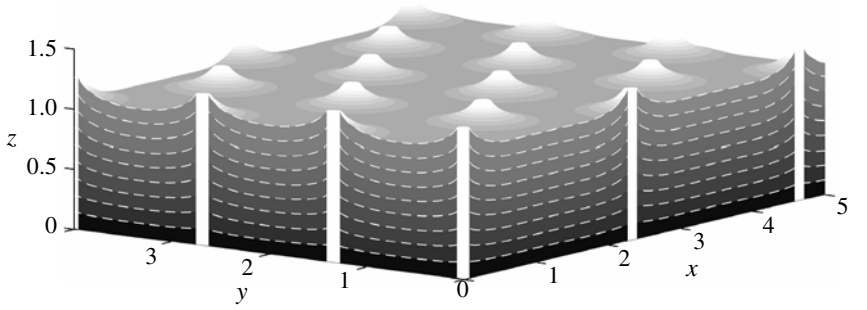

FIGURE 13. A hexagonal array of chimneys corresponding to mode I in figure 12. The thin white dashed curves are isotherms while thicker vertical white regions are chimneys.

flux (figure 12*d*). Under the maximum-flux criterion, there is a transition to a greater number of relatively weak chimneys as R_m increases (a transition to mode I at high R_m). This fact, as well as the observation that a much greater fraction of the volume flux occurs through the chimney in mode I, consistent with the formulation of the CAP model, leads us to expect that mode I will occur generically. Therefore, a hexagonal array of chimneys would have the form shown in figure 13, which is similar in appearance to the photograph of ammonium chloride solidifying in a rectangular tank by Huppert (1990), his figure 19(*c*).

6.4. *Results in axisymmetry: dependence on parameters*

6.4.1. *Application of the maximum-flux criterion*

We assume that the drainage area takes the value that maximizes the solute flux (§ 5). As in the planar case, we can satisfy this criterion by finding solutions for the active region that satisfy $\partial\gamma/\partial\delta = 0$. In § 6.1.1, we proved that the equations governing the active region depend on only two dimensionless groups: Ω and $E = R_m^2 \mathscr{D}\theta_\infty$. Therefore, under the maximum-flux criterion,

$$\mathscr{F}_{Solute} = -R_m \gamma_c(\Omega, E), \tag{6.20}$$

$$\mathscr{F}_{Heat} = -2\theta_\infty R_m \gamma_c(\Omega, E). \tag{6.21}$$

Figure 14 shows the behaviour of the proportionality function $\gamma_c(E, \Omega)$ in these equations, and can be used to derive and interpret the relationships between solute flux and Rayleigh number developed below.

6.5. *Relationships between solute fluxes and the mush Rayleigh number*

In axisymmetry, we find nonlinear relationships between solute flux and Rayleigh number, as shown in figure 15. The precise form of these relationships depends significantly on Ω, and somewhat more weakly on $\mathscr{D}$ and θ_∞. The departure from linearity arises from the different behaviour near the chimney, especially in terms of the geometric constriction of the flow discussed previously.

6.5.1. *Dependence on $\mathscr{D}$, θ_∞*

The Darcy number $\mathscr{D}$ and far-field temperature of the melt θ_∞ only appear multiplied together in the group $E = R_m^2 \mathscr{D}\theta_\infty$, so we need only consider the product $\mathscr{D}\theta_\infty$.

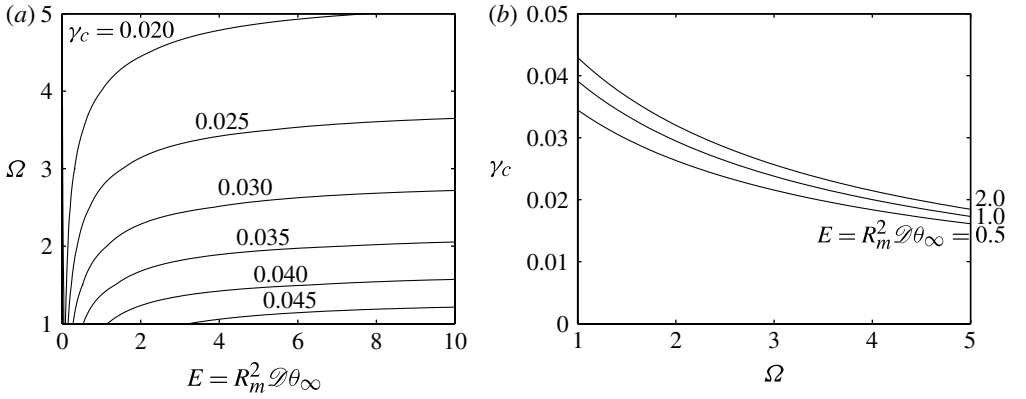

FIGURE 14. Behaviour of the proportionality constant $\gamma_c(E, \Omega)$ in (6.20) and (6.21). (*a*) Equally spaced contours of γ_c; note that they are approximately parallel to the E-axis at large E indicating that the γ_c depends principally on Ω in this region. (*b*) The dependence on Ω at three distinct values of E.

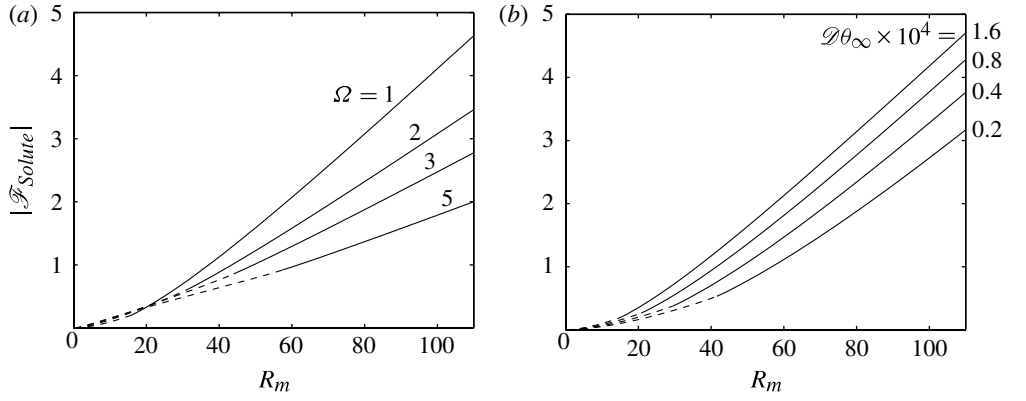

FIGURE 15. Relationships between solute flux and Rayleigh number in axisymmetry. (*a*) The relationships at different values of Ω for fixed $\mathscr{D}\theta_\infty = 1.4 \times 10^{-4}$. These become approximately linear at high R_m. In (*b*) we use different values of $\mathscr{D}\theta_\infty$ but fixed $\Omega = 1$. The solid parts of the curves correspond to mode I behaviour, and the dashed parts to mode II behaviour.

In the planar geometry $\mathscr{D}$ and θ_∞ did not affect the maximum flux at all. They do affect the chimney radius, which in axisymmetry controls the significance of geometric constriction, and hence they affect the solute flux (see (6.6*c*)).

Nevertheless, the slopes of the curves in figure 15(*b*) are approximately the same across a wide range of $\mathscr{D}\theta_\infty$ (we observe that this statement holds better at higher Ω, so figure 15(*b*) represents the 'worst-case scenario' $\Omega = 1$). Therefore, in some circumstances it is appropriate to seek an approximate relationship between flux and Rayleigh number that is independent of both $\mathscr{D}$ and θ_∞, a further major parametric simplification, as we now do.

6.5.2. *Dependence on* Ω

Both the degree of nonlinearity and the gradient of the slope of the graph of flux against Rayleigh number depend significantly on the value of Ω, as shown in figure 15(*a*). For low R_m, the flux does not depend strongly on Ω because to some extent the weaker convection caused by increasing Ω (as found in the planar case) is compensated by the lesser importance of geometrical constriction. However, at high R_m, when the smaller, weaker chimney mode of convection dominates, the solute flux is considerably lower at higher values of Ω. Indeed, at high R_m we can approximate the relationship between flux and Rayleigh number by a linear flux law

$$\mathscr{F}_{Solute} = R_m \tilde{\gamma}_c(\Omega) - c \quad \text{where } c \text{ is constant.} \tag{6.22}$$

The gradient $\tilde{\gamma}_c(\Omega)$ decreases with Ω, as shown by considering any of the curves in figure 14(*b*).

7. Concluding discussion and applications

Convection in a mushy layer can be modelled simply using a series of approximations which capture the underlying physics while reducing a two-dimensional problem (either planar or axisymmetric) to solving ordinary differential equations. In planar geometry, we deduced analytically that the solute and heat fluxes through the chimney are proportional to the mush Rayleigh number, with the proportionality depending on only one parameter. In axisymmetric geometry, we found that this proportionality function depended on two dimensionless groups Ω and $E = R_m^2 \mathscr{D}\theta_\infty$. This gave rise to the possibility of nonlinear relationships between the solute flux and the mush Rayleigh number R_m.

At a foundational level, nonlinearity arises from the presence of an additional length scale. The planar problem has only one length scale, the thermal length scale κ/V, and so on dimensional grounds the solute flux must be proportional to the Rayleigh number at high Rayleigh number. By contrast, in the axisymmetric problem geometrical constriction that occurs over a length scale that depends on the chimney radius introduces an additional length scale. Non-dimensionally, this means that the solute flux can depend on the Darcy number in axisymmetry, in which case there is a nonlinear relationship between solute flux and Rayleigh number.

Nevertheless, for large R_m and only moderate variation in $\mathscr{D}\theta_\infty$, this nonlinearity is weak. Furthermore we showed that the fully three-dimensional problem can be approximated well by an axisymmetric region of the same drainage area. Therefore we propose the *dimensional* approximations

$$\mathscr{F}_{Solute} \sim -V(C_0 - C_E) R_m \gamma_c(\Omega), \tag{7.1}$$

$$\mathscr{F}_{Heat} \sim -2\rho c_p V(T_\infty - T_0) R_m \gamma_c(\Omega). \tag{7.2}$$

For reference the non-dimensional parameters of the system are

$$R_m = \frac{\beta(C_0 - C_E) g \Pi_0}{\nu V}, \quad \mathscr{D} = \Pi_0 \frac{V^2}{\kappa^2}, \quad \theta_\infty = \frac{T_\infty - T_0}{T_0 - T_E}, \quad \Omega = 1 + \frac{\mathscr{L}}{(C_S - C_E)\Gamma c_p}. \tag{7.3}$$

The flux law (7.1) simplifies the parametric dependence of the solute flux caused by convection in a mushy layer. Solute flux depends quadratically on driving concentration difference $(C_0 - C_E)$ and linearly on permeability Π_0. It is independent of both the solidification rate V and the thermal diffusivity κ, which together set the overall thermal length scale κ/V.

Our modelling approach provides additional evidence of the robustness of the linear solute flux law in planar geometry, which was first proposed by Wells *et al.* (2010) on the basis of numerical work over a range of values of R_m and $\mathscr{C}$, holding θ_∞ and $\mathscr{S}$ constant (note that $\Omega = 1 + \mathscr{S}/\mathscr{C}$). In particular, we were able to find this law (at least for high R_m) across a broader range of parameter values.

Crucially, we were able to extend this approach into axisymmetry. The possibility of nonlinearity does suggest that caution should be used in applying the planar flux law to three-dimensional problems, and suggests that variation in $\mathscr{D}\theta_\infty$ should be moderate in order to do so.

It is also interesting to note that, for both geometries, we reproduce the ratio of solute flux to heat flux found by the scaling analysis of Worster (1991) and successfully used to explain the evolution of the melt region in experiments (Worster 1992*b*). That analysis left a factor in the flux laws undetermined, which did not affect the ratio. However, we improve on that study by determining this factor in terms of the non-dimensional parameters.

Furthermore, our approach demonstrates the need for a finite active region where baroclinic torque occurs in order to drive the entire convective flow through the chimneys. Our analytical approach also reveals the connection between straight-sided chimneys and a linear temperature field.

Although not capable of producing quantitative agreement with the direct numerical simulation of Chung & Worster (2002) and Wells *et al.* (2010), for reasons discussed earlier, our model does capture the same dynamics as numerical simulations. This suggests that it could be used as the basis of a dynamically informed parameterization of brine fluxes within and from sea ice. The types of simplification used in our model are consistent with current models for sea ice. These use a low vertical resolution (so a linear temperature profile is a reasonable approximation when only the bottom several centimetres of sea ice actively convect, as is typical) and also use an effective specific heat capacity, analogous to Ω.

Significantly, our model allows us to determine the vertical transport within the ice and hence also the bulk salinity, which is related to the interstitial concentration by

$$C_{bulk} = C(1-\phi) + C_S\phi \approx C(1-\phi), \tag{7.4}$$

since the concentration of the solid phase $C_S \approx 0$ in sea ice. Along with temperature, bulk salinity is the main state variable of interest to modellers. These results, which are the same in planar and axisymmetric geometry, could be applied to model the actively convecting region at the bottom of sea ice in a one-dimensional fashion, accounting for the effects of convection analytically. Within the passive region, where there is no horizontal variation, we find the *dimensional* result

$$w = -VR_m w_c \zeta, \tag{7.5}$$

where ζ, which equals z/h_0 in our formulation, in general denotes the ratio of the distance into the convecting region to the depth of that region, and the appropriate interstitial concentration difference ΔC in the Rayleigh number is that across the convecting layer only. Then using the full equation of salt conservation in steady state,

$$-V\frac{\partial C_{bulk}}{\partial z} = -w\frac{\partial C}{\partial z} \quad \Rightarrow \quad C_{bulk} = C_0 - \frac{R_m \Delta C}{2}\left(1-\zeta^2\right) w_c. \tag{7.6}$$

The solid fraction could then by determined by inverting (7.4). In this paper, we have calculated w_c from our model, both in the planar case (in which it depends on Ω), and in the axisymmetric case (in which it depends on Ω and E in general). However,

in practice it would be appropriate to treat w_c as an adjustable parameter, tuned by experimental data or numerical simulation. This could provide a way to account for factors not incorporated into our model, such as differences in the thermal properties of the phases and a non-uniform permeability.

We have shown how to produce a parameterization of heat and solute fluxes through chimneys based on a Rayleigh number that governs the strength of convection. A Rayleigh number could be defined for the actively convecting region near the base of growing sea ice and the flux law or structure of the interstitial flow field that we have found could be used to compute salt transport both within and from the ice, as well as the solid fraction. This would lead to a simple model of sea ice whose salt content is dynamically determined.

Acknowledgement

The authors would like to thank D. Notz, A. J. Wells and J. S. Wettlaufer for helpful comments and corrections to an earlier draft of this paper.

Supplementary material

Supplementary material is available at journals.cambridge.org/flm.

Appendix. Scaling for the chimney width with power-law far-field temperature profile

In previously unpublished work by J. Ashmore & M. G. Worster, scaling relationships were discovered between the shape of the vertical temperature variation in a mushy layer and the width of a chimney as follows.

Consider an isolated chimney in an infinite (both vertically and horizontally) mushy layer. Look for a boundary-layer similarity solution of heat conservation (2.10) and the vorticity equation (2.7) with far-field conditions

$$\theta \to cz^b, \quad \psi_x \to 0 \quad (x \to \infty). \tag{A 1}$$

In the boundary layer, the dominant balances in (2.10) and (2.7) become

$$\Omega(-\psi_z\theta_x + \psi_x\theta_z) \sim \theta_{xx}, \quad \psi_{xx} \sim -R_m\theta_x. \tag{A 2}$$

This is analogous to our active region. There is a similarity solution

$$\psi = \left(\frac{cR_m}{b\Omega}\right)^{1/2} z^{(1+b)/2}\,\Psi(\eta), \quad \theta = cz^b\Theta(\eta), \quad \eta = \frac{x}{d(z)}, \quad d(z) = \frac{z^{(1-b)/2}}{(bcR_m\Omega)^{1/2}}, \tag{A 3}$$

where Ψ and Θ satisfy ordinary differential equations that can be readily solved.

As in (3.7), we substitute the similarity solution to find that the average concentration in the chimney is $\overline{C} \sim cz^b\Theta_0(1+b)/(1+3b)$. Recalling (2.11*c*) for mass conservation, we substitute the similarity solution and neglect the final term as asymptotically small in the limit $\mathscr{D} \to 0$ to find

$$a \sim \frac{\mathscr{D}^{1/3}}{(cR_m\Omega)^{1/6}} z^{(1-b)/6}\alpha(b), \quad \text{where } \alpha(b) = \left(\frac{3\Psi_0(1+3b)}{b^{1/2}\left((1+3b)\Psi_0' + 2b\Theta_0\right)}\right)^{1/3}. \tag{A 4}$$

Therefore $a \propto z^{(1-b)/6}$ and so straight-sided chimneys correspond precisely to linear ($b = 1$) far-field temperature profiles. Note that (A 4) reduces to (3.8) if $b = 1$ and

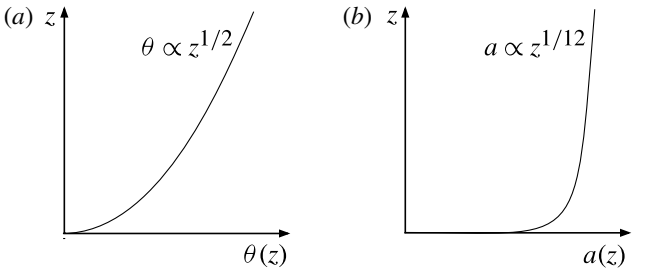

FIGURE 16. A nonlinear far-field temperature profile (a), where $b = 1/2$, gives rise to the chimney width shown in (b). The sides remain very steep apart from near the base. Its shape is qualitatively similar to the numerical results of Chung & Worster (2002).

$c = 1/h_0$. However, we can also find the shape of the chimney with other power laws for the far-field temperature. Figure 16 shows the case $b = 1/2$ for example, and illustrates the fact that the chimney is typically almost straight-sided except near its base for a variety of realistic temperature profiles.

REFERENCES

BECKERMANN, C. & WANG, C. Y. 1995 Multiphase/-scale modelling of alloy solidification. In *Annual Reviews of Heat Transfer* (ed. C. L. Tien), vol. 6, pp. 115–198. Begell House.

BOETTINGER, W. J., WARREN, J. A., BECKERMANN, C. & KARMA, A. 2002 Phase-field simulation of solidification. *Annu. Rev. Mater. Res.* **32** (1), 163–194.

CHUNG, C. A. & WORSTER, M. G. 2002 Steady-state chimneys in a mushy layer. *J. Fluid Mech.* **455**, 387–411.

COPLEY, S. M., GIAMEI, A. F., JOHNSON, S. M. & HORNBECKER, M. F. 1970 The origin of freckles in unidirectionally solidified castings. *Metall. Trans.* **1**, 2193–2204.

FELTHAM, D. L., UNTERSTEINER, N., WETTLAUFER, J. S. & WORSTER, M. G. 2006 Sea ice is a mushy layer. *Geophys. Res. Lett.* **33** (14).

FOWLER, A. C. 1985 The formation of freckles in binary alloys. *IMA J. Appl. Maths* **35** (2), 159–174.

HILLS, R. N., LOPER, D. E. & ROBERTS, P. H. 1983 A thermodynamically consistent model of a mushy zone. *Q. J. Mech. Appl. Mech.* **36** (4), 505–540.

HUNKE, E. C., NOTZ, D., TURNER, A. K. & VANCOPPENOLLE, M. 2011 The multiphase physics of sea ice: a review for model developers. *Cryosphere* **5** (4), 989–1009.

HUPPERT, H. E. 1990 The fluid mechanics of solidification. *J. Fluid Mech.* **212**, 209–240.

HUPPERT, H. E. & WORSTER, M. G. 1985 Dynamic solidification of a binary melt. *Nature* **314** (6013), 703–707.

HUPPERT, H. E. & WORSTER, M. G. 2012 Flows involving phase change. In *Handbook of Environmental Fluid Dynamics* (ed. H. J. Fernando). Taylor and Francis (in press).

LAPWOOD, E. R. 1948 Convection of a fluid in a porous medium. *Proc. Camb. Phil. Soc.* **44** (4), 508–521.

NOTZ, D. & WORSTER, M. G. 2008 In situ measurements of the evolution of young sea ice. *J. Geophys. Res.* **113**, doi:10.1029/2007JC004333.

NOTZ, D. & WORSTER, M. G. 2009 Desalination processes of sea ice revisited. *J. Geophys. Res.* **114**, doi:10.1029/2008JC004885.

OERTLING, A. B. & WATTS, R. G. 2004 Growth of and brine drainage from NaCl–H_2O freezing: a simulation of young sea ice. *J. Geophys. Res.* **109**, doi:10.1029/2001JC001109.

PEPPIN, S. S. L., AUSSILLOUS, P., HUPPERT, H. E. & WORSTER, M. G. 2007 Steady-state mushy layers: experiments and theory. *J. Fluid Mech.* **570**, 69–77.

PETRICH, C., LANGHORNE, P. & EICKEN, H. 2011 Modelled bulk salinity of growing first-year sea ice and implications for ice properties in spring. In *Proc. 21st Intl Conf. on Port and Ocean Engineering under Arctic Conditions (POAC), Montreal, Canada*, pp. 1–10. POAC11–187 (electronic).

SCHULZE, T. P. & WORSTER, M. G. 1998 A numerical investigation of steady convection in mushy layers during the directional solidification of binary alloys. *J. Fluid Mech.* **356**, 199–220.

SCHULZE, T. P. & WORSTER, M. G. 1999 Weak convection, liquid inclusions and the formation of chimneys in mushy layers. *J. Fluid Mech.* **388**, 197–215.

UNTERSTEINER, N. 1968 Desalination processes of sea ice revisited. *J. Geophys. Res.* **74**, 1251–1257.

VANCOPPENOLLE, M., GOOSSE, H., DE MONTETY, A., FICHEFET, T., TREMBLAY, B. & TISON, J.-L. 2010 Modelling brine and nutrient dynamics in Antarctic sea ice: the case of dissolved silica. *J. Geophys. Res.* **115**, doi:10.1029/2009JC005369.

WELLS, A. J., WETTLAUFER, J. S. & ORSZAG, S. A. 2010 Maximal potential energy transport: a variational principle for solidification problems. *Phys. Rev. Lett.* **105**, 254502.

WETTLAUFER, J. S., WORSTER, M. G. & HUPPERT, H. E. 1997 Natural convection during solidification of an alloy from above with application to the evolution of sea ice. *J. Fluid Mech.* **344**, 291–316.

WORSTER, M. G. 1991 Natural convection in a mushy layer. *J. Fluid Mech.* **224**, 335–359.

WORSTER, M. G. 1992*a* Instabilities of the liquid and mushy regions during solidification of alloys. *J. Fluid Mech.* **237**, 649–669.

WORSTER, M. G. 1992*b* The dynamics of mushy layers. In *Interactive Dynamics of Convection and Solidification*, *NATO ASI Series*, vol. E219,. pp. 113–138. Kluwer.

WORSTER, M. G. 1997 Convection in mushy layers. *Annu. Rev. Fluid Mech.* **29** (1), 91–122.

WORSTER, M. G. 2000 Solidification of fluids. In *Perspectives in Fluid Dynamics: a Collective Introduction to Current Research* (ed. G. K. Batchelor, H. K. Moffatt & M. G. Worster). pp. 393–446. Cambridge University Press.